# THE STABILITY OF CYLINDRICAL SHELLS CONVEYING VISCOUS FLOW

M. HEIL*

*Department of Applied Mathematics, University of Leeds*
*Leeds, LS2 9JT, U.K.*

This paper examines the stability of cylindrical shells conveying viscous flow. Geometrically nonlinear Lagrangian shell theory is used to describe the deformation of the tube wall. The fluid flow is modelled using lubrication theory. The coupled fluid–solid problem is discretized with finite differences and the critical parameter combinations (upstream pressure and volume flux) for which the tube buckles are examined. The most unstable circumferential buckling wavenumber and the buckling modes are determined for an experimental procedure in which the upstream pressure is held at a constant value while the volume flux is increased until buckling occurs. Finally, the effect of variations in the tube geometry and the effects of the axial pre-stretch are examined.

© 1996 Academic Press Limited

## 1. INTRODUCTION

THE PROBLEM OF FLOW THROUGH COLLAPSIBLE tubes has been studied both theoretically and experimentally by many authors [for a recent review see Kamm & Pedley (1989)]. The main motivation for this work comes from the investigation of certain biological flows such as blood flow in veins and arteries or air flow in the bronchial airways during forced expiration.

A typical experimental set-up is shown in Figure 1. Inside a pressure chamber, a finite-length collapsible tube is mounted on two rigid tubes, and viscous fluid is pumped through. Various combinations of parameters can be varied in the experiments (e.g., external pressure and volume flux or external pressure and upstream pressure, etc.). For sufficiently large external pressure and/or volume flux, the tube collapses at the downstream end, i.e. it buckles nonaxisymmetrically [see Conrad (1969), Katz *et al.* (1969) or Elad *et al.* (1992)]. Following the collapse, large amplitude self-excited oscillations can be observed for a wide range of parameters.

So far, most theoretical models of the complex interaction between fluid and solid mechanics have used relatively simple ''tube laws'' to describe the elastic behaviour of the tube wall. These tube laws relate the cross-sectional area of the tube to the local transmural pressure-difference. The fluid flow was either modelled one-dimensionally or *ad hoc* assumptions about the shape of the deformed cross-sectional area had to be made (Wild *et al.* 1977).

To derive a more realistic model of the fluid–solid interaction in this problem it is necessary to develop an improved description of the wall mechanics. Therefore, Heil & Pedley (1995a) used geometrically nonlinear shell theory to describe the deformation of the tube wall. They used lubrication theory to model the fluid flow and developed a FEM code to study the axisymmetric prebuckling deformation of the tube. Meanwhile,

* Present Address: Room 3-260, Department of Mechanical Engineering, Massachusetts Institute of Technology, Cambridge, MA 02139, U.S.A.
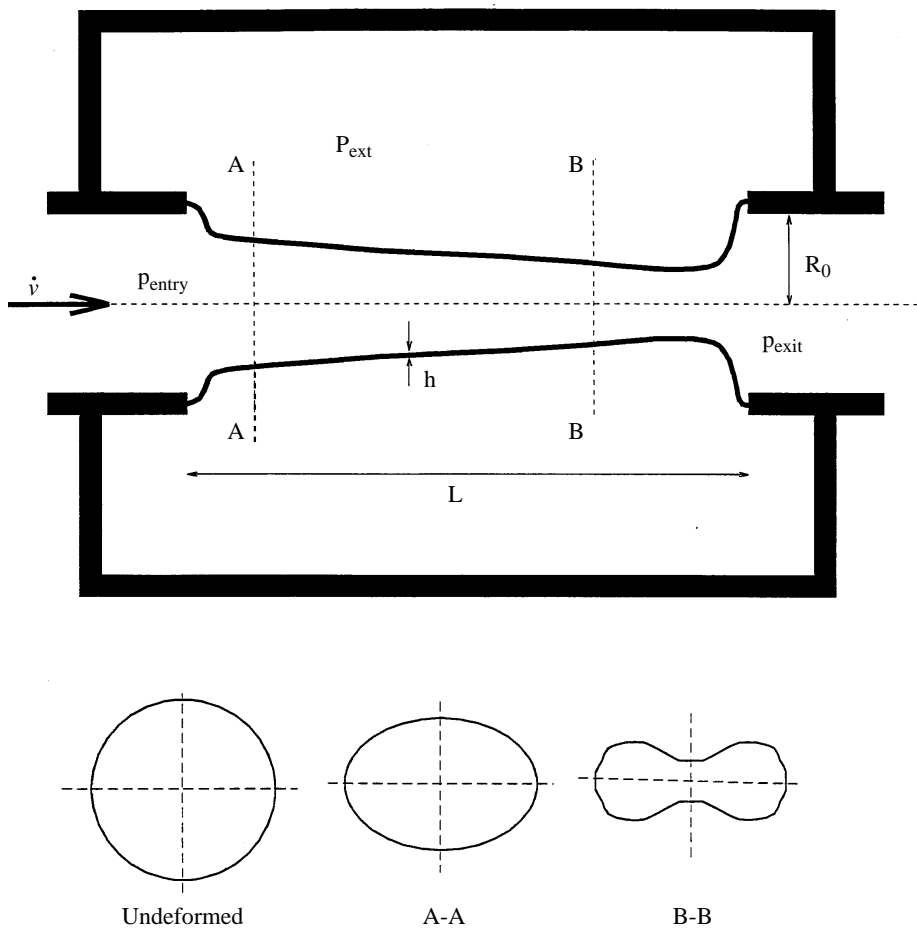
Figure 1. Sketch of the model problem.

this code has been extended to study the large displacement postbuckling deformation of the collapsed tube (Heil & Pedley 1995b).

The stability analysis, presented in this paper, forms a link between the steady pre- and postbuckling deformation. We investigate the linear stability of the axisymmetric tube to establish the critical parameter combinations (e.g. volume flux and external pressure) for which the axisymmetric deformation of the tube loses its stability by divergence.

We use the same fluid and solid models as in Heil & Pedley (1995a), i.e. geometrically nonlinear shell theory and lubrication theory. The governing equations are derived from the principle of virtual displacements and they are discretized with finite differences. The equations for the pre-buckling displacements are solved with a Newton-Raphson method. A secant Newton method is used to determine the critical parameters (upstream pressure, volume flux and axial pre-stretch) for which the axisymmetric tube becomes unstable.

We analyse the buckling mechanism corresponding to an experimental procedure in which the fluid pressure at the upstream end of the collapsible tube is held constant while the volume flux is increased until buckling occurs. The effects of variations in the tube geometry and the effects of axial pre-stretch are studied.

This approach differs from previous work, e.g. by Paidoussis and co-workers [an extensive review of which is given in Paidoussis & Li (1993)], who were primarily interested in the flutter instability of cylindrical shells. They used linear shell equations (mostly Flügge's equations) coupled to an inviscid potential flow to determine the growth rate of traveling wave disturbances to the shell. It is interesting to note that, in spite of their fundamentally different fluid model, they found that clamped–clamped shells lose their stability by divergence (buckling), followed by flutter (a Hopf bifurcation) at a slightly higher flow rate (Paidoussis & Denise 1972). This led to the proposition that the large displacement self-excited oscillations observed in the experiments could be: (a) flutter instabilities, or (b) '"periodic divergence", with the antinodes snapping through alternately between the positive and negative extremes of the modal form involved' (Paidoussis & Li 1993; p. 186).

The latter view is supported by Conrad's (1969) experiments. Figure 4 in his paper shows a sequence of photographs of partially and fully collapsed rubber tubes conveying a viscous flow and Conrad reports that "these configurations could be maintained as long as desired" (p. 286)—clearly indicating that the collapse was not necessarily coupled to a flutter instability. Further support for the latter view is given by Conrad's observation that "during oscillation, the motion of the walls of the tube was essentially a succession, within a limited range, of the steady flow collapse states . . ." (p. 291).

## 2. THE MODEL

### 2.1. Shell Theory

We model the tube of length $L$, undeformed radius $R_0$ and wall thickness $h$ as a cylindrical shell and describe its deformation using a geometrically nonlinear Kirchhoff/Love type shell theory [e.g. Wempner (1973)]. Using the usual assumptions (thickness of the shell is constant, normals to the undeformed mid-plane remain normal), the deformation of the shell can be expressed in terms of the mid-plane displacements $\tilde{\boldsymbol{v}}$. We use Lagrangian coordinates $\tilde{x}^\alpha$ (Greek and Latin indices have values 1,2 and 1,2,3, respectively, and the summation convention is used) to parameterize the shell mid-plane. A tilde is used to distinguish dimensional variables from their nondimensionalized equivalents.

Let $\tilde{\boldsymbol{r}}^0(\tilde{x}^\alpha)$ be the vector to a material point on the mid-plane before deformation. We choose cylindrical coordinates as the Lagrangian coordinates ($\tilde{x}^1$ and $\tilde{x}^2$ are the arc lengths in the axial and circumferential direction, respectively; see Figure 2). Lower case letters refer to the undeformed reference state and the superscript 0 indicates the vector to the mid-plane. Thus,

$$\tilde{\boldsymbol{r}}^0 = (R_0 \sin(\tilde{x}^2/R_0),\ R_0 \cos(\tilde{x}^2/R_0),\ \tilde{x}^1)^{\mathrm{T}}, \qquad \tilde{x}^1 \in [0, L], \qquad \tilde{x}^2 \in [0, 2\pi R_0]. \qquad (1)$$

The position of an arbitrary point in the shell at a distance $\tilde{x}^3$ from the mid-plane can be written as

$$\tilde{\boldsymbol{r}} = \tilde{\boldsymbol{r}}^0 + \tilde{x}^3 \boldsymbol{n}, \qquad \tilde{x}^3 \in [-h/2, h/2]; \qquad (2)$$

$\boldsymbol{n} = \boldsymbol{a}_3$ is the unit vector normal to the two mid-plane base vectors $\boldsymbol{a}_\alpha = \tilde{\boldsymbol{r}}^0_{,\alpha}$ where the comma denotes partial differentiation with respect to $\tilde{x}^\alpha$. Let $a_{\alpha\beta} = \boldsymbol{a}_\alpha \cdot \boldsymbol{a}_\beta$ be the covariant mid-plane metric tensor, $a$ its determinant and $\tilde{b}_{\alpha\beta} = \boldsymbol{n} \cdot \boldsymbol{a}_{\alpha,\beta}$ the curvature tensor of the undeformed mid-plane. After deformation, the material point on the mid-plane with the Lagrangian coordinates $\tilde{x}^\alpha$ has been displaced to a new position $\tilde{\boldsymbol{R}}^0(\tilde{x}^\alpha) = \tilde{\boldsymbol{r}}^0(\tilde{x}^\alpha) + \tilde{\boldsymbol{v}}(\tilde{x}^\alpha)$. We decompose the displacement vector, $\tilde{\boldsymbol{v}}$, into the
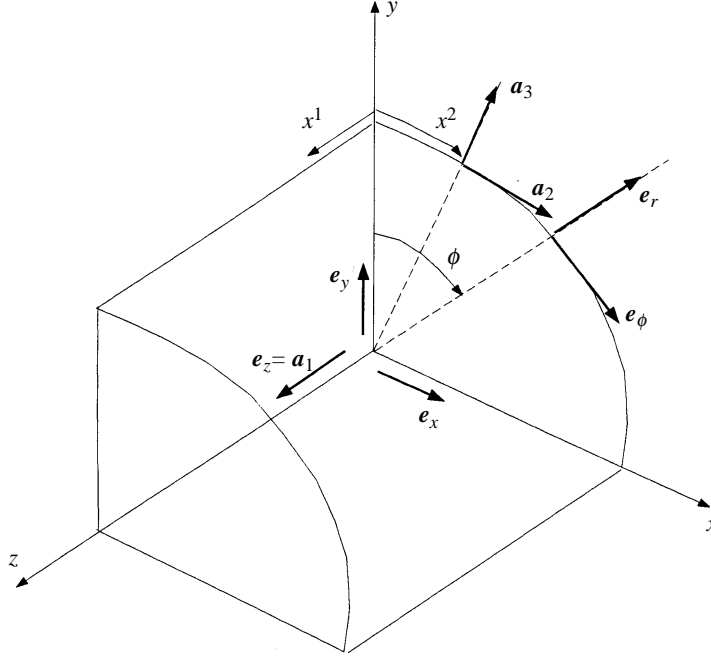
Figure 2. Sketch of the Lagrangian and Eulerian coordinate systems used in the analysis.

undeformed basis, $\tilde{\boldsymbol{v}} = \tilde{v}^j \boldsymbol{a}_j$. We use capital letters for the quantities associated with the deformed tube: mid-plane base vectors $\boldsymbol{A}_\alpha = \tilde{\boldsymbol{R}}^0_{,\alpha}$, unit normal $\boldsymbol{N} = \boldsymbol{A}_3$, mid-plane metric tensor $A_{\alpha\beta} = \boldsymbol{A}_\alpha \cdot \boldsymbol{A}_\beta$, curvature tensor $\tilde{B}_{\alpha\beta} = \boldsymbol{N} \cdot \boldsymbol{A}_{\alpha,\beta}$, and vector to a point in the deformed shell

$$\tilde{\boldsymbol{R}} = \tilde{\boldsymbol{R}}^0 + \tilde{x}^3 \boldsymbol{N}. \tag{3}$$

The tangent vectors on the inner surface of the deformed shell at $\tilde{x}^3 = -h/2$ are given by $\boldsymbol{G}_\alpha = \tilde{\boldsymbol{R}}_{,\alpha}$ and the area differential $\mathrm{d}\mathscr{A}$ on this surface is

$$\mathrm{d}\mathscr{A} = \sqrt{G}\, \mathrm{d}\tilde{x}^1\, \mathrm{d}\tilde{x}^2, \tag{4}$$

where $G$ is the determinant of the off mid-plane metric tensor $G_{\alpha\beta} = \boldsymbol{G}_\alpha \cdot \boldsymbol{G}_\beta$.

The deformation is described by the strain tensor $\gamma_{\alpha\beta} = \frac{1}{2}(A_{\alpha\beta} - a_{\alpha\beta})$ and the bending tensor $\tilde{\kappa}_{\alpha\beta} = -(\tilde{B}_{\alpha\beta} - \tilde{b}_{\alpha\beta})$. In spite of the large deformations, the strain of the shell is still relatively small [Elad *et al.* (1992) report about 2–3% maximum extension in their experiments], therefore we use Hooke's law (linear constitutive equations) and Love's first approximation to express the strain energy function, $\tilde{\phi}$, (strain energy per unit area of the undeformed mid-plane of the shell) in terms of the strain and bending tensors:

$$\tilde{\phi} = \frac{1}{2} h \tilde{E}^{\alpha\beta\gamma\delta} \left( \gamma_{\alpha\beta} \gamma_{\gamma\delta} + \frac{1}{12} h^2 \tilde{\kappa}_{\alpha\beta} \tilde{\kappa}_{\gamma\delta} \right) \tag{5}$$

with the plane stress stiffness tensor

$$\tilde{E}^{\alpha\beta\gamma\delta} = \frac{E}{2(1+\nu)} \left( \alpha^{\alpha\gamma} a^{\beta\delta} + a^{\alpha\delta} a^{\beta\gamma} + \frac{2\nu}{1-\nu} a^{\alpha\beta} a^{\gamma\delta} \right), \tag{6}$$

where $E$ is Young's modulus, $\nu$ is Poisson's ratio and $a^{\alpha\beta}$ is the contravariant metric tensor of the undeformed mid-plane, $a^{\alpha\beta} a_{\beta\gamma} = \delta^\alpha_\gamma$.

We use the principle of virtual displacements,

$$\delta\Pi_{\text{strain}} - \delta\Pi_{\text{load}} = 0, \tag{7}$$

where $\delta\Pi_{\text{strain}}$ is the variation of the strain energy stored in the deformed tube wall and $\delta\Pi_{\text{load}}$ is the work done by the load $\tilde{f}$, acting on the tube surface, during a virtual displacement. We nondimensionalize the coordinates $\tilde{x}^i$, the displacements $\tilde{v}$ and the bending tensor $\tilde{\kappa}_{\alpha\beta}$ with the undeformed radius, $\tilde{x}^j = x^i R_0$, $\tilde{v} = v R_0$, $\tilde{k}_{\alpha\beta} = \kappa_{\alpha\beta}/R_0$ and the stiffness tensor and the loads with Young's modulus, $\tilde{E}^{\alpha\beta\gamma\delta} = E^{\alpha\beta\gamma\delta}E$ and $\tilde{f} = fE$. The strain tensor, $\gamma_{\alpha\beta}$, is already dimensionless. Then the variation of the strain energy is given by

$$\delta\Pi_{\text{strain}} = \int_0^{2\pi} \int_0^{L/R_0} \left(\frac{h}{R_0}\right)\left[E^{\alpha\beta\gamma\delta}\left(\gamma_{\alpha\beta}\delta\gamma_{\gamma\delta} + \frac{1}{12}\left(\frac{h}{R_0}\right)^2 \kappa_{\alpha\beta}\delta\kappa_{\gamma\delta}\right)\right]\sqrt{a}\,dx^1\,dx^2, \tag{8}$$

where the variations of strain and bending tensor have to be taken with respect to the displacements $v^i$ and their derivatives.

In Heil & Pedley (1995a) we compared the exact, fully nonlinear expressions for the strain and bending tensors to the simplified expressions which were derived in Sanders' (1963) first-order nonlinear moderate rotation theory. We found that for large pre-buckling deformations Sanders' theory could be improved considerably by using the exact expression for the strain tensor, $\gamma_{\alpha\beta}$, while using Sanders' linearized expressions for the bending tensor, $\kappa_{\alpha\beta}$. The resulting nonlinear partial differential equations are only slightly more complicated than those derived in Sanders' original theory since the main complication arises from the nonlinearity in the bending tensor. This approach allows us to investigate cases where the tube upstream end is subject to a high internal pressure. In these cases, the pre-buckling deformation of the tube can be large enough to make relevant those nonlinearities in the strain tensor, which were neglected by Sanders. The moderate rotation assumption, leading to the linearization of the bending tensor, is still valid in these cases.

Hence, we use Sanders' expression for the bending tensor, i.e.

$$\kappa_{11} = -v^3_{,11}, \tag{9}$$

$$\kappa_{12} = \kappa_{21} = -v^3_{,12} + \frac{3}{4}v^2_{,1} - \frac{1}{4}v^1_{,2}, \tag{10}$$

$$\kappa_{22} = -v^3_{,22} + v^2_{,2}. \tag{11}$$

The numerical results presented in Heil & Pedley (1995b) confirm that this linearized bending tensor yields accurate results for the initial stages of the nonaxisymmetric buckling deformation of the tube.

For the purposes of linear stability analysis, we linearize the exact nonlinear strain tensor with respect to the buckling displacements (for the axisymmetric pre-buckling deformation we have $v^2 = 0$ and $\partial/\partial x^2 = 0$), i.e.

$$\gamma_{11} = v^1_{,1} + \frac{1}{2}[(v^1_{,1})^2 + (v^3_{,1})^2], \tag{12}$$

$$\gamma_{12} = \gamma_{21} = \frac{1}{2}[(1 + v^3)v^2_{,1} + (v^3_{,2} - v^2)v^3_{,1} + (v^1_{,1} + 1)v^1_{,2}], \tag{13}$$

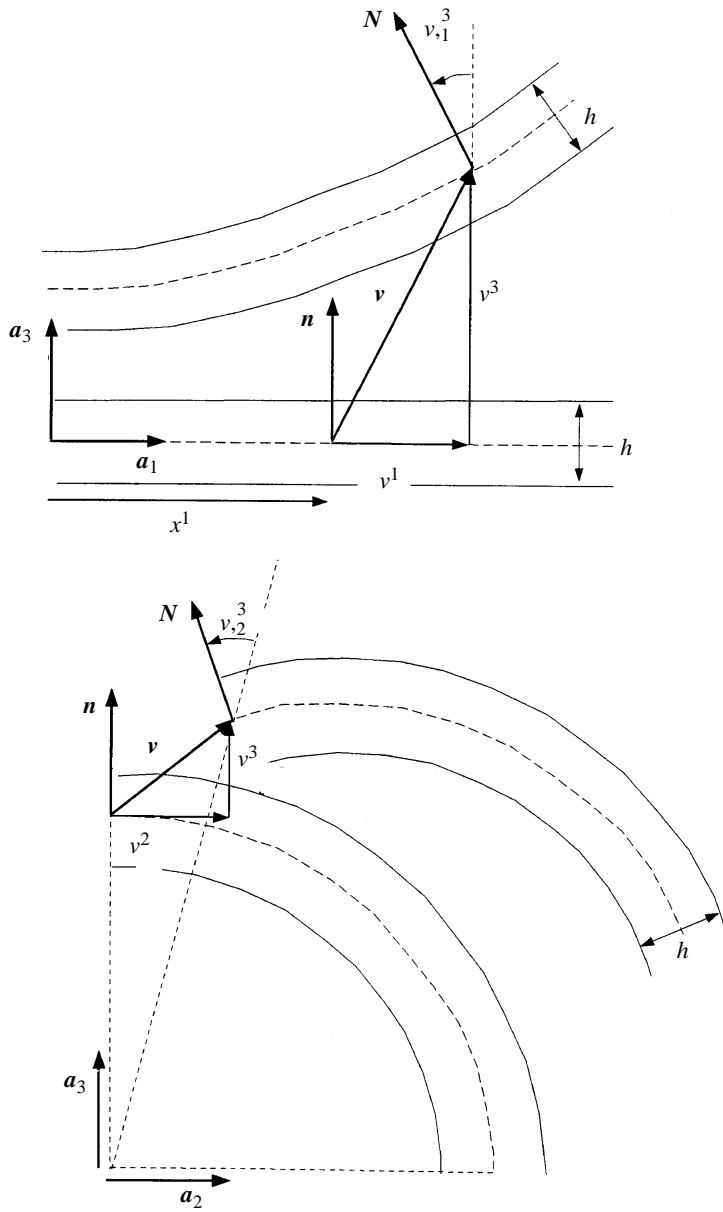$$\gamma_{22} = \frac{1}{2}[2v^2_{,2} + 2(v^2_{,2} + 1)v^3 + (v^3)^2]. \tag{14}$$

Figure 3. The tube deformation under the moderate rotation assumption.

For moderate rotations of the tube wall, the tube geometry changes as sketched in Figure 3. The components $I^i$ of the nondimensional vector $\boldsymbol{I} = I^i \boldsymbol{a}_i$ to a point on the inside of the deformed tube are

$$I^1 = x^1 + v^1 + \frac{h}{2R_0} v^3_{,1}, \qquad I^2 = v^2\left(1 - \frac{h}{2R_0}\right) + \frac{h}{2R_0} v^3_{,2} \quad \text{and} \quad I^3 = 1 + v^3 - \frac{h}{2R_0}. \qquad (15)$$

The inside of the tube forms the boundary of the fluid domain. We use the nondimensional Lagrangian coordinates $x^\alpha$ to parametrize the Eulerian cylindrical polar coordinates $(r, z, \varphi) = (\tilde{r}/R_0, \tilde{z}/R_0, \varphi)$ of this boundary. The $z$-coordinate of a

point on the tube inner surface is equal to the projection of $I$ on the tube's centre line, i.e.

$$z = I \cdot a_1 = x^1 + v^1 + \frac{h}{2R_0} v_{,1}^3. \tag{16}$$

The Eulerian tube radius is given by

$$R = \sqrt{I \cdot I - z^2} = \sqrt{\left(v^2\left(1 - \frac{h}{2R_0}\right) + \frac{h}{2R_0} v_{,2}^3\right)^2 + \left(1 + v^3 - \frac{h}{2R_0}\right)^2}, \tag{17}$$

and the Eulerian polar angle of a point on the tube wall is

$$\tan \varphi = \frac{I \cdot e_x}{I \cdot e_y} = \frac{\left[v^2\left(1 - \frac{h}{2R_0}\right) + \frac{h}{2R_0} v_{,2}^3\right]\cos(x^2) + \left[1 + v^3 - \frac{h}{2R_0}\right]\sin(x^2)}{-\left[v^2\left(1 - \frac{h}{2R_0}\right) + \frac{h}{2R_0} v_{,2}^3\right]\sin(x^2) + \left[1 + v^3 - \frac{h}{2R_0}\right]\cos(x^2)}. \tag{18}$$

These transformations provide an Eulerian description of the fluid domain in terms of the shell coordinates $x^\alpha$ and the mid-plane displacement field $v^i(x^\alpha)$. In Section 2.2 we shall use these transformations to determine the fluid traction in the Eulerian basis $f_{\text{fluid}} = f_r e_r + f_z e_z + f_\varphi e_\varphi$, where the Eulerian base vectors are given by $e_r = (\sin \varphi, \cos \varphi, 0)^T$, $e_z = (0, 0, 1)^T$, $e_\varphi = (\cos \varphi, -\sin \varphi, 0)^T$. Since the traction exerted by the fluid on the wall is opposite to the traction exerted by the wall on the fluid, the load acting on the tube wall is $f = -f_{\text{fluid}}$. We decompose $f$ into the undeformed base vectors $a_i$, $f = f^i a_i$. The load components $f_i$ are then given by

$$f^i = -(f_z e_z \cdot a^i + f_r e_r \cdot a^i + f_\varphi e_\varphi \cdot a^i), \tag{19}$$

where the $a^i$ are the contravariant mid-plane base vectors, given by $a^i \cdot a_j = \delta_j^i$. The fluid traction acts on area elements $d\mathscr{A}$ on the inside of the tube. Therefore, the work done by the fluid traction during a virtual displacement $\delta R|_{x^3 = -(h/2R_0)} = \delta I = \delta I^i a_i$ is equal to

$$\delta \Pi_{\text{load}} = \int_0^{2\pi} \int_0^{L/R_0} f^i \delta I_i \sqrt{G} \,|_{x^3 = -(h/2R_0)} \, dx^1 \, dx^2. \tag{20}$$

Again the variations have to be carried out with respect to the displacements and their derivatives, e.g.

$$\delta I_1 = \delta v^1 + \frac{h}{2R_0} \delta v_{,1}^3 \tag{21}$$

etc. We set the pressure, $p_{\text{ext}}$, in the pressure chamber to zero (a transmural pressure difference can be created by changing the fluid pressure). Then the load on the outside of the tube is zero and does not contribute to the virtual work done during the deformation.

We insert (8) and (20) into (7) and combine the terms which are multiplied by the same displacement variations. This transforms (7) into a variational equation of the form

$$\int_0^{2\pi} \int_0^{L/R_0} (\phi_i \delta v^i + \phi_{i\alpha} \delta v_{,\alpha}^i + \phi_{i\alpha\beta} \delta v_{,\alpha\beta}^i) \, dx^1 \, dx^2, \tag{22}$$

where the $\phi$-terms depend on the load terms $f^i$ and on the displacements $v^i$ and their first and second derivatives with respect to the Lagrangian coordinates $x^\alpha$. Partial

integration transforms (22) into the following system of three partial differential equations

$$\mathcal{F}_i = \phi_i - \phi_{i\alpha,\alpha} + \phi_{i\alpha\beta,\alpha\beta} = 0. \tag{23}$$

The algebraic manipulations involved in the last two steps are straightforward but rather lengthy, therefore they were carried out using the symbolic formula manipulator *REDUCE*. The boundary conditions are obtained naturally during the partial integration. In the experiment described above, the tube is clamped at both ends and the displacements have to be periodic in the circumferential direction; at $x^1 = 0$ and $x^1 = L/R_0$ the displacements have to be prescribed (which allows the possibility of pre-stretch) and we have $dv^3/dx^1 = 0$.

For the purpose of the stability analysis we consider small nonaxisymmetric disturbances $v_B^i(x^1, x^2)$ to the axisymmetric pre-buckling deformation $v_A^i(x^1)$. We separate the buckling displacements into mode shapes $V_B^i(x^1)$ and trigonometric functions, i.e.

$$[v_B^1, v_B^2, v_B^3] = [V_B^1(x^1)\cos(Nx^2), V_B^2(x^1)\sin(Nx^2), V_B^3(x^1)\cos(Nx^2)], \tag{24}$$

where $N$ is the circumferential buckling wavenumber. Linearization of the transformations (16) to (18) between the Eulerian and Lagrangian coordinates with respect to the buckling displacements yields

$$z = x^1 + v_A^1 + \frac{h}{2R_0}v_{A,1}^3 + \left(V_B^1 + \frac{h}{2R_0}V_{B,1}^3\right)\cos(Nx^2), \tag{25}$$

$$R = 1 + v_A^3 - \frac{h}{2R_0} + V_B^3\cos(Nx^2), \tag{26}$$

and

$$\varphi = x^2 + \frac{V_B^2[1 - (h/2R_0)] - NV_B^3(h/2R_0)}{1 + v_A^3 - (h/2R_0)}\sin(Nx^2). \tag{27}$$

## 2.2. Fluid Mechanics

For physiologically realistic values of the Reynolds number (Pedley 1980), the fluid mechanics would be governed by the full Navier Stokes equations. If we assume, however, that the product of Reynolds number and wall slope in the streamwise direction ($\alpha$, say) and the wall slope itself are small everywhere, we can simplify the equations considerably. The small wall slope assumption is justifiable in the context of the stability analysis since we are only concerned with the initial stages of the buckling for which the tube is not yet severely collapsed at the downstream end.

We use Eulerian cylindrical polar coordinates (see Figure 2) for the fluid flow and base the Reynolds number on the average axial fluid velocity $\bar{U}$, i.e. $\text{Re} = \bar{U}R_0/\nu$, where $\nu$ is the kinematic viscosity of the fluid. Under the assumption $\alpha \ll 1$, the equation of continuity provides a scaling for the velocity components, $\bar{u}_r/\bar{u}_z$, $\bar{u}_\varphi/\bar{u}_z = \mathcal{O}(\alpha) \ll 1$. Using this scaling and the assumption $\text{Re}\,\alpha \ll 1$ in the momentum equations shows that, at leading order, the fluid pressure, $\tilde{p}$ is only a function of the axial coordinate $\tilde{z}$, $\tilde{p} = \tilde{p}(\tilde{z})$.

We scale the $z$-component of the velocity as $\bar{u}_z = u_z\dot{V}/R_0^2$, where $\dot{V}$ is the volume flux through the tube, and nondimensionalize the pressure with Young's modulus, $\tilde{p} = pE$. Then the $z$-component of the momentum equation reduces to

$$\frac{\partial p}{\partial z} = q\,\frac{\pi R_0}{8L}\,\nabla^2 u_z, \tag{28}$$

where $\nabla^2$ stands for the nondimensional Laplace operator in the $(r,\varphi)$-plane. The parameter $q$ represents the nondimensional pressure drop through an undeformed tube of length $L$ and inner radius $R_0$,

$$q = \frac{8\mu\dot{V}L}{\pi R_0^4 E}, \tag{29}$$

and it is proportional to the volume flux. The parabolic equation (28) is subject to the normalization condition

$$\int_{A(z)} u_z \, dA = 1, \tag{30}$$

which requires that the same volume flux, $\dot{V}$, passes through every cross-section $A(z)$ and to a no-slip boundary condition on the tube walls,

$$u_z \,|_{\partial A} = 0. \tag{31}$$

At one $z$-coordinate, an initial value for the pressure has to be prescribed, e.g. $p(z = 0) = p_{\text{entry}}$. Physically, these equations imply that the flow through every cross-section $A(z)$ is identical to the flow through an infinitely long tube of the same constant cross-section.

The fluid stress vector, $t$, at the tube wall can be obtained from the stress tensor $\underline{T}$ and the normal vector $N$,

$$t = \underline{T} \cdot N, \tag{32}$$

where the normal vector $N$ is the third base vector on the shell surface, $N = G_3 = A_3$. Using the moderate rotation assumption as illustrated in Figure 3, we write the normal vector as

$$N = e_r - v_{,1}^3 e_z - v_{,2}^3 e_\varphi. \tag{33}$$

Inserting the velocity scalings, derived above, into the stress tensor $\underline{T}$ for a Newtonian fluid in cylindrical polar coordinates and nondimensionalizing all stresses with Young's modulus $E$, we obtain the following approximation for the components of the stress vector $t_{\text{fluid}} = t_r e_r + t_z e_z + t_\varphi e_\varphi$:

$$t_r = -p, \quad t_z = p v_{,1}^3 + \tau_w \quad \text{and} \quad t_\varphi = p v_{,2}^3. \tag{34}$$

The nondimensional wall shear stress $\tau_w$ is given by

$$\tau_w = q \frac{\pi R_0}{8L} \frac{\partial u_z}{\partial n}, \tag{35}$$

where $\partial/\partial n$ stands for the normal derivative in the $(r,\varphi)$-plane.

The displacement derivatives in (34) reflect the change in the direction of the fluid traction during the buckling. Due to the fluid–solid interaction, the pressure and the wall shear stress depend on the wall displacements as well. The fluid equations, which determine the fluid traction, have to be solved in the slightly buckled tube, the description of which is based on the Lagrangian coordinates, $x^\alpha$. Therefore, we will now transform the fluid equations into Lagrangian coordinates.

During the axisymmetric pre-buckling deformation of the tube, particles on the inside of the tube wall with the Lagrangian coordinate $x^1$ (which were on a level $z_{\text{undef}} = x^1$ in the undeformed tube) are displaced to the new axial position

$$z_{\text{axisym}}(x^1) = x^1 + v_A^1 + \frac{h}{2R_0} v_{A,1}^3 \tag{36}$$

and they remain in one plane. We use this relation to establish a mapping between Eulerian and Lagrangian coordinates before the buckling and express the pressure gradient in terms of the axial Lagrangian coordinate $x^1$, i.e.

$$\frac{dp}{dz} = \frac{1}{1 + v_{A,1}^1 + (h/2R_0)v_{A,11}^3} \frac{dp}{dx^1}. \tag{37}$$

During the buckling, the axial component of the buckling displacement moves material points with the coordinate $x^1$ out of the plane $z = z_{\text{axisym}}(x^1)$; material points with different $x^1$-coordinates move into the plane $z = z_{\text{axisym}}(x^1)$ and the radius and the polar angle of material points in the cross-section $z = z_{\text{axisym}}(x^1)$ are no longer functions of the circumferential Lagrangian coordinate $x^2$ alone. However, this can be shown to be a second-order effect (see Appendix) which allows us to neglect the warping of the cross-sections in the linear stability analysis.

We denote the radius of the unbuckled tube by $\rho_A = 1 + v_A^3 - h/2R_0$ and denote the amplitude of the radial buckling displacement by $V_B^3 = \varepsilon \ll 1$. Then the radius and polar angle to a point on the tube wall in the cross-section $z = z_{\text{axisym}}(x^1)$ are given by

$$R_{\text{tube}} = \rho_A + \varepsilon \cos(Nx^2), \tag{38}$$

$$\varphi = x^2 + \varepsilon \frac{(V_B^2/V_B^3)[1 - (h/2R_0)] - (h/2R_0)N}{\rho_A} \sin(Nx^2). \tag{39}$$

To solve the Poisson equation (28) in the slightly buckled cross-section we construct a body-fitted coordinate system involving the circumferential Lagrangian coordinate $x^2$. For this purpose we change the coordinates in the cross-section from the Eulerian cylindrical polar coordinates $(r, \varphi)$ to $(\rho, x^2)$ by using (39) and by writing the radius, $r$, as

$$r = \rho(\rho_A + \varepsilon \cos(Nx^2)]. \tag{40}$$

The new coordinate system is illustrated in Figure 4 and the sketch shows that the
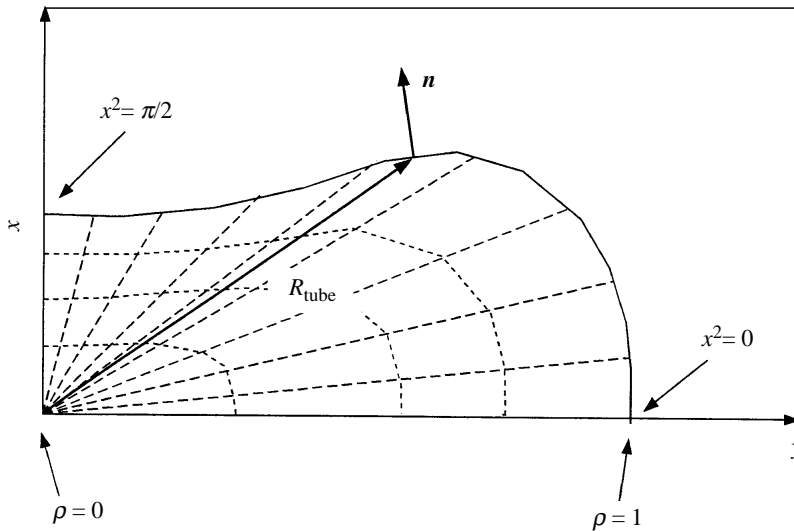


Figure 4. The body-fitted coordinate system $(\rho, x^2)$ in the buckled cross-section. The dashed lines are the isolines $x^2 = \text{const.}$ and $\rho = \text{const.}$

transformation is one-to-one even for relatively large buckling deformations. The Jacobian of the mapping is given by

$$\mathscr{J} = \frac{\partial r}{\partial \rho}\frac{\partial \varphi}{\partial x^2} - \frac{\partial r}{\partial x^2}\frac{\partial \varphi}{\partial \rho} = \rho_A + \varepsilon\left[1 + N\left(\left(1 - \frac{h}{2R_0}\right)\frac{V_B^2}{V_B^3} - \frac{h}{2R_0}N\right)\right]\cos(Nx^2) + \mathcal{O}(\varepsilon^2). \quad (41)$$

The curvilinear boundary of the fluid domain is thus transformed into the line $\rho = 1$.

We transform the Laplace operator to the new coordinates and expand the velocity field, $u_z$, and the pressure gradient, $dp/dz$, in powers of the buckling amplitude, $\varepsilon$,

$$u_z = u_{z0} + \varepsilon u_{z1} + \ldots \quad (42)$$

and

$$\frac{dp}{dz} = \frac{dp_0}{dz} + \varepsilon\frac{dp_1}{dz} + \ldots \quad (43)$$

The zero*th* order equation is the equation for the flow in the unbuckled tube,

$$\frac{\partial^2 u_{z0}}{\partial \rho^2} + \frac{1}{\rho}\frac{\partial u_{z0}}{\partial \rho} + \frac{1}{\rho^2}\frac{\partial^2 u_{z0}}{\partial(x^2)^2} = \frac{8\rho_A^2 L}{\pi q R_0}\frac{dp_0}{dz}, \quad (44)$$

the solution of which, subject to the boundary condition $u_z|_{\rho=1} = 0$, is a Poiseuille flow in the mapped plane, i.e.

$$u_{z0} = -\frac{2\rho_A^2(1 - \rho^2)L}{\pi q R_0}\frac{dp_0}{dz}. \quad (45)$$

Inserting this into the first-order equation yields an equation for the perturbation velocity $u_{z1}$,

$$\frac{\partial^2 u_{z1}}{\partial \rho^2} + \frac{1}{\rho}\frac{\partial u_{z1}}{\partial \rho} + \frac{1}{\rho^2}\frac{\partial^2 u_{z1}}{\partial(x^2)^2} = \frac{4L}{\pi q R_0}\left[2\rho_A^2\frac{dp_1}{dz} - \rho_A(N^2 - 4)\cos(Nx^2)\frac{dp_0}{dz}\right], \quad (46)$$

which has the solution

$$u_{z1} = -\frac{2\rho_A^2(1 - \rho^2)L}{\pi q R_0}\frac{dp_1}{dz} + \frac{4L\rho_A}{\pi q R_0}(\rho^2 - \rho^N)\frac{dp_0}{dz}\cos(Nx^2). \quad (47)$$

The pressure gradients are determined by imposing the normalization condition (30) in the transformed coordinates, i.e.

$$\dot{V} = \dot{V}_0 + \varepsilon V_1 + \ldots = \int_0^{2\pi}\int_0^1 u_z[\rho_A + \varepsilon\cos(Nx^2)]\mathscr{T}\,d\rho\,dx^2 = 1. \quad (48)$$

Normalization of the velocity field $u_{z0}$, i.e. $\dot{V}_0 = 1$, yields

$$\frac{dp_0}{dz} = -\frac{qR_0}{\rho_A^4 L}. \quad (49)$$

We assume that the upstream pressure and the volume flux are held at a constant value during the buckling. Then the condition $\dot{V}_1 = 0$, inserted into (48), forces the disturbance pressure gradient to vanish and we have

$$p_1 = \frac{dp_1}{dz} = 0. \quad (50)$$

This is closely related to the fact that at leading order the cross-sectional area of the buckled tube remains constant.

Finally, we work out the wall shear stress $\tau_w = \tau_{w0} + \varepsilon \tau_{w1} + \ldots$ The vector to a point on the tube wall is

$$\boldsymbol{R}_{\text{tube}} = [R_x, R_y]^{\text{T}} = [\rho_A + \varepsilon \cos(Nx^2)][\sin(\varphi(x^2)), \cos(\varphi(x^2))]^{\text{T}}, \tag{51}$$

where $\varphi(x^2)$ is given by (39). The normal vector on the tube wall is obtained from

$$n = \frac{1}{\sqrt{\left(\dfrac{\mathrm{d}R_x}{\mathrm{d}(x^2)}\right)^2 + \left(\dfrac{\mathrm{d}R_y}{\mathrm{d}(x^2)}\right)^2}} \left[ -\frac{\mathrm{d}R_y}{\mathrm{d}(x^2)}, \frac{\mathrm{d}R_x}{\mathrm{d}(x^2)} \right]^{\text{T}}. \tag{52}$$

After transforming the Cartesian components of $\nabla = (\partial/\partial x, \partial/\partial y)^{\text{T}}$ to $\rho$ and $x^2$, we expand $\partial u_z/\partial n = \boldsymbol{n} \cdot \nabla u_z$ in powers of $\varepsilon$ and obtain

$$\tau_{w0} = -\frac{qR_0}{2\rho_A^3 L} \tag{53}$$

and

$$\tau_{w1} = \frac{q(N-1)R_0}{2\rho_A^4 L} \cos(Nx^2). \tag{54}$$

The last equation shows that the wall shear stress is reduced where the tube is bulging out and increased where the tube is collapsing, as one would expect.


## 3. THE GOVERNING EQUATIONS

The governing equations are obtained by inserting the expressions for the wall shear stress into the load terms in the three shell equations $\mathscr{F}_i = 0$. While the wall shear stress is directly related to the shell's displacement field, the pressure distribution is governed by the fourth equation,

$$\mathscr{F}_4 = \frac{\partial p}{\partial x^1} + \left(1 + v_{A,1}^1 + \frac{h}{2R_0} v_{A,11}^3\right) \frac{qR_0}{\left(1 + v_A^3 - \dfrac{h}{2R_0}\right)^4 L} = 0, \tag{55}$$

which is obtained from (37) and (49).

The tube is subject to an axial pre-stretch, which changes its length from $L$ to $L + U$. Denoting this pre-stretch by $\varepsilon_U = U/R_0$, we obtain the following boundary conditions for the displacements:

$$v^1 |_{x^1=0} = -\frac{\varepsilon_U}{2} \quad \text{and} \quad v^1 |_{x^1=L/R_0} = \frac{\varepsilon_U}{2}, \tag{56}$$

$$v^3 |_{x^1=0} = v^3 |_{x^1=L/R_0} = 0 \quad \text{and} \quad v_{,1}^3 |_{x^1=0} = v_{,1}^3 |_{x^1=L/R_0} = 0. \tag{57}$$

The fluid pressure is prescribed at the upstream end of the tube, i.e.

$$p |_{x^1=0} = p_{\text{entry}}. \tag{58}$$

Before the buckling, the tube deformation is axisymmetric and the displacement field depends only on the $x^1$-coordinate. We insert $v^i(x^\alpha) = v_A^i(x^1)$ with $v_A^2(x^1) = 0$ into the shell equations $\mathscr{F}_i = 0$ and obtain two ordinary differential equations for the pre-buckling displacements $v_A^1(x^1)$ and $v_A^3(x^1)$. The equation for equilibrium in the

circumferential direction, $\mathscr{F}_2 = 0$, is fulfilled automatically. The pressure distribution is governed by (55).

To derive the equations for the buckling deformation, we insert $v^i(x^1, x^2) = v^i_A(x^1) + v^j_B(x^1, x^2)$ into the shell equations $\mathscr{F}_i = 0$. Since we are only interested in the linear stability, we linearize with respect to the buckling displacements and use the ansatz (24). This leads to a system of linear ordinary differential equations of the form

$$\mathscr{L}_i = \sum_{k=0}^{4} L_{ijk} \frac{\partial^k V^j_B}{\partial (x^1)^k} = 0, \tag{59}$$

where the coefficients $L_{ijk}$ are functions of the pre-buckling displacement $v^i_A(x^1)$ and the pressure distribution $p(x^1)$. As shown in the last section, the pressure distribution remains unchanged during the buckling. The buckling modes $V^i_B(x^1)$ are subject to the eight homogeneous boundary conditions

$$V^i_B |_{x^1=0} = V^i_B |_{x^1=L/R_0} = 0 \quad \text{and} \quad V^3_{B,1} |_{x^1=0} = V^3_{B,1}|_{x^1=L/R_0} = 0. \tag{60}$$

## 4. THE NUMERICAL SOLUTION

### 4.1. THE AXISYMMETRIC PRE-BUCKLING DEFORMATION

We discretize the equations by replacing the derivatives with respect to $x^1$ by second-order accurate finite differences on a uniformly spaced mesh with spacing $h_{FD} = L/(N_{FD}R_0)$ (Almroth 1966). We denote the discretized pre-buckling displacements by $v^i_A |_{x^1=(Jh_{FD})} = \mathscr{V}^i_{A(J)}$. Then the derivatives at $x^1 = Jh_{FD}$ $(J = 0, \dots, N_{FD})$ are approximated by standard central differences. The highest derivatives of the axial and radial displacements are $v^1_{A,11}$ and $v^3_{A,1111}$, respectively. Discretization of the two shell equations $\mathscr{F}_1 = 0$ and $\mathscr{F}_3 = 0$ at the $N_{FD} + 1$ nodes $J = 0, \dots, N_{FD}$ yields $2(N_{DF} + 1)$ nonlinear algebraic equations which involve the $2(N_{FD} + 1)$ unknowns within the domain. Due to the discretization of the highest derivatives at the end-points of the domain, they also make reference to the six "virtual" gridpoints $\mathscr{V}^3_{A(-2)}$, $\mathscr{V}^1_{A(-1)}$, $\mathscr{V}^3_{A(-1)}$, $\mathscr{V}^1_{A(N_{FD}+1)}$, $\mathscr{V}^3_{A(N_{FD}+1)}$ and $\mathscr{V}^3_{A(N_{FD}+2)}$. Discretization of the six boundary conditions (56) and (57) provides the final six equations.

Discretization of the pressure gradient in (55) using central differences, i.e.

$$\frac{dp}{dx^1} = \frac{\mathscr{P}_{(J+1)} - \mathscr{P}_{(J-1)}}{2h_{FD}} \tag{61}$$

at nodes $J = 1, \dots, N_{FD}$, generates $N_{FD}$ equations involving the $N_{FD} + 2$ unknowns $\mathscr{P}_{(0)}, \dots, \mathscr{P}_{(N_{FD}+1)}$. Prescribing the pressure at the upstream end yields only one additional equation, $\mathscr{P}_{(0)} = p_{\text{entry}}$, and it can also be shown that the even and odd numbered pressure variables remain uncoupled in this scheme. The "missing" additional equation which links all pressure variables is obtained by integrating (55) analytically between $x^1 = L/R_0$ and $x^1 = L/R_0 + h_{FD}$. Since this part of the domain is inside the rigid support where $v^i = 0$ we obtain

$$\frac{\mathscr{P}_{(N_{FD}+1)} - \mathscr{P}_{(N_{FD})}}{h_{FD}} = -\frac{qR_0}{(1 - h/2R_0)^4 L}, \tag{62}$$

where we assumed that the inner radius of the downstream support is equal to the inner radius of the undeformed tube.

This transforms the ordinary differential equations and the boundary conditions into a system of $3N_{FD} + 10$ nonlinear algebraic equations. The system of equations can readily be solved using the Newton-Raphson technique which enables us to compute the axisymmetric pre-buckling displacements for a wide range of parameters, i.e. $\mathcal{V}^i_{A(J)}(q, p_{\text{entry}}, \varepsilon_U)$.

## 4.2. The Buckling Deformation

We discretize the three buckling equations (59), using standard second order central finite differences for the pre-buckling displacements $\mathcal{V}^i_{A(J)}$ and for the buckling displacements $\mathcal{V}^i_{B(J)}$ at the $N_{FD} + 1$ gridpoints $J = 0, \ldots, N_{FD}$. This yields $3(N_{FD} + 1)$ linear algebraic equations which involve the $3(N_{FD} + 1)$ discretized buckling displacements at $J = 0, \ldots, N_{FD}$ and eight "virtual" gridpoints $\mathcal{V}^3_{B(-2)}$, $\mathcal{V}^1_{B(-1)}$, $\mathcal{V}^2_{B(-1)}$, $\mathcal{V}^3_{B(-1)}$, $\mathcal{V}^1_{B(N_{FD}+1)}$, $\mathcal{V}^2_{B(N_{FD}+1)}$, $\mathcal{V}^3_{B(N_{FD}+1)}$ and $\mathcal{V}^3_{B(N_{FD}+2)}$. The eight additional equations are obtained by discretizing the eight displacement boundary conditions (60). This yields a system of $3N_{FD} + 11$ homogeneous linear algebraic equations for the discretized buckling displacements $\mathcal{V}^i_{B(J)}$, which we write symbolically as

$$\mathfrak{B}V = 0, \tag{63}$$

where $\mathfrak{B}$ is the $(3N_{FD} + 11) \times (3N_{FD} + 11)$ buckling matrix and $V$ stands for the vector of the buckling displacements. The coefficients of the buckling matrix $\mathfrak{B}$ depend on the wavenumber $N$ of the buckling mode and on the pre–buckling displacements $\mathcal{V}^i_{A(J)}$ which are functions of the parameters $q$, $p_{\text{entry}}$ and $\varepsilon_U$. The buckling equations have a non-trivial solution if the determinant of the buckling matrix vanishes, i.e.

$$\det \mathfrak{B} = 0. \tag{64}$$

This is a condition for the parameter combinations $(N, q, p_{\text{entry}}, \varepsilon_U)$ for which the axisymmetric deformation of the tube becomes unstable.

## 4.3. Tracing of the Critical Parameter Combinations

To compute the critical parameter combinations in the form $q_{\text{crit}}(N, p_{\text{entry}}, \varepsilon_U)$ we use a secant Newton method based on the method proposed in Press *et al.* (1992):
 (i) choose $N$, $p_{\text{entry}}$ and $\varepsilon_U$;
 (ii) start with an initial guess $q_0$ for $q_{\text{crit}}$;
(iii) compute the value of the corresponding buckling determinant, $d_0 = \det \mathfrak{B}(q_0, p_{\text{entry}}, \varepsilon_U)$;
(iv) set $q_1 = 1 \cdot 05 q_0$ and compute the value of the corresponding buckling determinant, $d_1 = \det \mathfrak{B}(q_1, p_{\text{entry}}, \varepsilon_U)$;
 (v) extrapolate

$$q_2 = q_0 - \frac{q_1 - q_0}{d_1 - d_0} d_0;$$

(vi) compute the value of the buckling determinant at the new value, $d_2 = \det \mathfrak{B}(q_2, p_{\text{entry}}, \varepsilon_U)$;
(vii) choose the new $q_0$ and $q_1$ from the old $q_0$, $q_1$ and $q_2$, such that either
     (a) the root remains bracketed between the new $q_0$ and $q_1$ or
     (b) the new $q_0$ and $q_1$ are the values closest to the root;
(viii) go to (v) until convergence.
The determinant of the buckling matrix $\mathfrak{B}$ can easily be determined by computing its

LU-decomposition and by multiplying the diagonals of the upper triangular factor. It should be noted that the absolute value of the determinant is irrelevant since it can easily be scaled by multiplying the matrix by an arbitrary factor (which does not make the matrix "more singular"). Therefore, the determinants were scaled with the value of the first $d_0$ computed during the above iteration (scaling of the determinant is also necessary to avoid overflow during the multiplication of the diagonal elements). The convergence criterion for the iteration was based on the change of subsequent values of $q_{\text{crit}}$. The iteration was stopped when

$$\left| \frac{q_2 - q_\alpha}{q_\alpha} \right| \leq \varepsilon_{\text{det}} \quad \text{for } \alpha = 0,1, \tag{65}$$

where $\varepsilon_{det} = 10^{-5}$ proved to be a good choice. For this value, the above scheme typically reduced the determinant of the buckling matrix by a factor of $10^{-10}$ in 10 to 15 iterations.

This procedure was embedded in an outer loop which increased $p_{\text{entry}}$ and thereby traced the entire path of critical parameters for a fixed geometry.

Having established the critical parameter combination and computed the approximately singular buckling matrix, the buckling modes were determined from (63) by Gauss-Jordan elimination with pivoting (Lowe 1994). For an exactly singular matrix this procedure transforms the original buckling matrix $\mathfrak{B}$ into an upper triangular matrix, the last row of which contains only zero entries. The magnitude of the largest nonzero entry in the last row of the transformed matrix can be used as an indicator of "how singular" the buckling matrix is. In the computations, it was typically of the order of the machine precision. After assigning an arbitrary value to the last component of the buckling vector $V$ and discarding the last equation, the remaining $3N_{FD} + 10$ equations were solved for the remaining buckling displacements by backsubstitution.

### 4.4. CODE VALIDATION AND PERFORMANCE

The code was validated by performing a number of tests. Firstly, the FD-solution of the pre-buckling equations was compared to the numerical solution obtained from the FEM program, described in Heil & Pedley (1995a). The two independent numerical codes were in perfect agreement.

Then the code was used to predict the buckling loads of cylindrical shells of various geometries under constant external pressure, $q = 0$. Table 1 compares the predictions for the buckling loads for tubes under constant internal pressure, obtained with the FD

TABLE 1

Comparison of the predictions for the critical buckling pressures for zero volume flux. For all cases $v = 0.3$ was used. $p_{\text{crit}}^{\text{Yamaki}}$ is the buckling pressure obtained from diagram 2·12 in Yamaki (1984)

| $L/R_0$ | $h/R_0$ | $N_{\text{buckl}}$ | $p_{\text{crit}}^{\text{FD}}$ | $p_{\text{crit}}^{\text{Yamaki}}$ | Difference (%) |
|---------|---------|---------|---------|---------|---------|
| 10 | 1/50 | 3 | $-7.38 \times 10^{-6}$ | $-7.40 \times 10^{-6}$ | 0·3 |
| 30 | 1/50 | 2 | $-2.49 \times 10^{-6}$ | $-2.44 \times 10^{-6}$ | 2·0 |
| 50 | 1/50 | 2 | $-2.25 \times 10^{-6}$ | $-2.22 \times 10^{-6}$ | 1·3 |
| 10 | 1/100 | 3 | $-1.43 \times 10^{-6}$ | $-1.42 \times 10^{-6}$ | 0·7 |
| 30 | 1/100 | 2 | $-4.04 \times 10^{-7}$ | $-4.16 \times 10^{-7}$ | 2·8 |
| 50 | 1/100 | 2 | $-2.93 \times 10^{-7}$ | $-2.92 \times 10^{-7}$ | 0·3 |

code to the predictions based on a Galerkin solution of Flügge's equations [taken from diagram 2.12 in Yamaki (1984)].

Finally, the critical parameter combinations, predicted by this code, were compared to the values obtained from the large displacement FEM code which was developed to examine the postbuckling behaviour (Heil & Pedley 1995b). For a given value of the upstream pressure the predictions for the critical volume flux differed by less than 3%.

The computations presented in the next sections were carried out with 150 equally spaced FD-nodes. To check for mesh convergence, some of the computations were repeated using 300 nodes. The critical parameter combinations obtained with the two different discretizations differed by less than 0·05%.

The computations were carried out on a Silicon Graphics Challenge/XL computer with R4400 processors. A typical iteration to determine the critical value of the volume flux required about 450 s of CPU time for each combination of $N, p_{entry}$ and $\varepsilon_U$ when using a discretization with 150 FD-nodes.

## 5. RESULTS AND DISCUSSION

The computations presented here were carried out with $L/R_0 = 10$ and $L/R_0 = 20$, respectively, $h/R_0 = 1/20$ and $v = 0.49$. This corresponds to a nondimensional bending stiffness of

$$K = \frac{1}{12(1 - v^2)} \left(\frac{h}{R_0}\right)^3 = 1.37 \times 10^{-5}. \tag{66}$$

Poisson's ratio and relative wall thickness were chosen to be in the range of parameters in the experiments of Elad *et al.* (1992), where (by the standards of shell theory) relatively thick-walled rubber tubes had been used.

We investigate the buckling mechanism corresponding to the following experimental procedure: we keep the external pressure, $p_{ext} = 0$, and the fluid pressure at the upstream end of the collapsible segment, $p_{entry}$, at a constant value while we increase the volume flux, $q$, slowly until buckling occurs. This procedure could be realised experimentally by connecting the upstream end of the tube to a large reservoir and by controlling the volume flux with a volumetric pump, connected to the downstream end of the collapsible segment.

For zero volume flux, the entire tube is subject to a constant transmural pressure $p_{entry}$. The tube buckles if $p_{entry}$ falls below a critical negative value $p_{entry(crit)}$. For the geometries considered here, the most unstable buckling mode has $N = 2$ waves in the circumferential direction. The axisymmetric pre-buckling deformation and the most unstable buckling mode are symmetric in the axial direction.

If we set the upstream pressure to a value greater than $p_{entry(crit)}$, then the tube deformation for zero volume flux is axisymmetric. A nonzero volume flux creates a viscous pressure drop in the fluid and thereby increases the compressive load on the tube wall in the direction of the flow. The corresponding axisymmetric deformation reduces the tube cross-sectional area which increases the pressure drop even further. For a certain volume flux $q_{crit}$, the compressive load reaches a critical value for which the axisymmetric deformation of the tube becomes unstable. The buckling is initiated at the downstream end, where the compressive load has its largest value.

If we increase the upstream pressure $p_{entry}$, then the tube can sustain a higher viscous pressure drop until the downstream end is under sufficiently strong compression to initiate the buckling. Therefore, an increase in the upstream pressure leads to an increase in the critical volume flux $q_{crit}$. This effect is enhanced by the fact that a
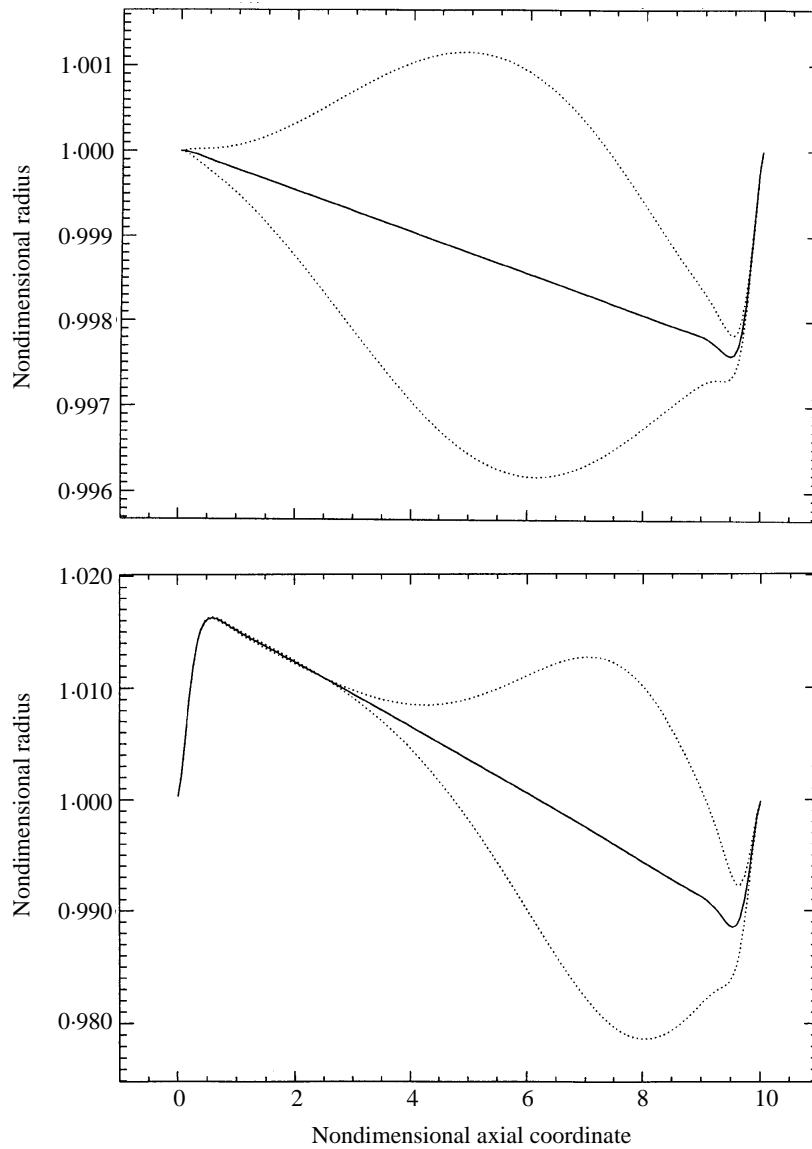
Figure 5. The axisymmetric pre-buckling deformation at the onset of buckling and, superimposed, the corresponding buckling mode for $N = 2$. Note the different scales in the radial direction. $L/R_0 = 10$, $\varepsilon_U = 0$. Upper figure: $p_{\text{entry}} = 2 \cdot 0 \times 10^{-6}$ and $q_{\text{crit}} = 1 \cdot 49 \times 10^{-4}$. Lower figure: $p_{\text{entry}} = 2 \cdot 45 \times 10^{-3}$ and $q_{\text{crit}} = 3 \cdot 46 \times 10^{-3}$.

higher upstream pressure reduces the tube's compressive deformation and thereby reduces the tube resistance.

Figure 5 shows the pre-buckling deformation, $v_A^i$, (solid line) and, superimposed, the corresponding buckling deformation, $v_A^i \pm V_B^i$, (dotted lines) for two critical parameter combinations $(p_{\text{entry}}, q_{\text{crit}})$ and for $N = 2$. The amplitude of the buckling modes was scaled such that the maximum radial displacement of the buckling deformations $V_B^3$ had the same value as the maximum radial pre-buckling displacement $v_A^3$. In the upper figure the tube is subject to a small upstream pressure, $p_{\text{entry}} = 2 \cdot 0 \times 10^{-6}$, the lower figure corresponds to a tube under a high upstream pressure, $p_{\text{entry}} = 2 \cdot 45 \times 10^{-3}$. The
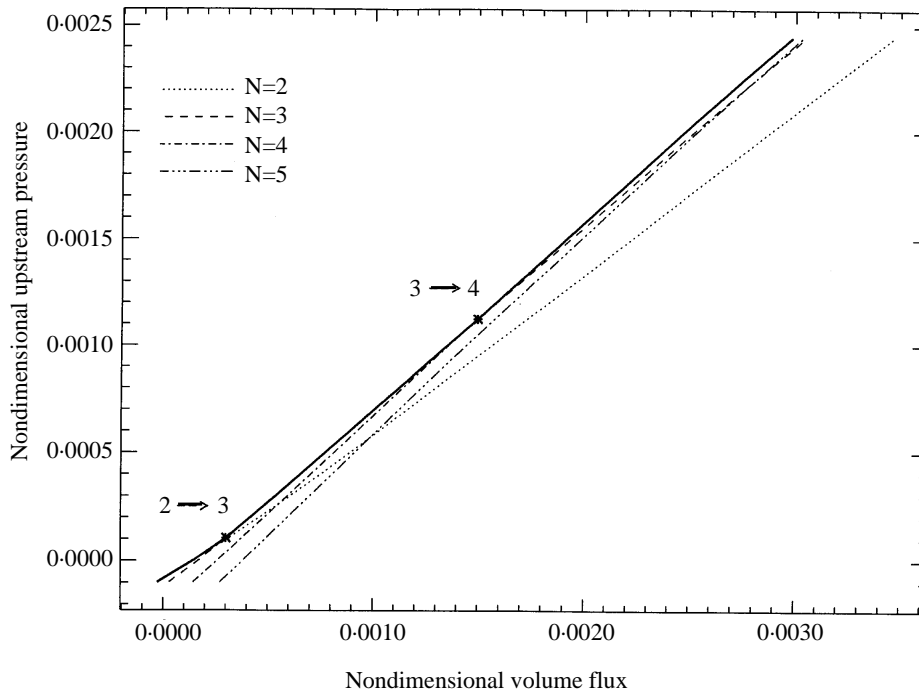
Figure 6. The critical parameter combinations for a tube with $L/R_0 = 10$. The thin broken lines represent the critical values for wavenumbers $N = 2, \ldots, 5$. The most unstable combination is indicated by the thick solid line. The markers indicate the transition to a new most unstable wavenumber.

plots show, that an increase in upstream pressure confines the buckling to the compressed part of the tube near the downstream end.

This has an important implication: since under these conditions only a fraction of the tube is involved in the buckling, the buckling process becomes increasingly similar to the buckling of a shorter tube. The distended upstream part of the tube merely acts as a support for the downstream part which is under compression. As is well known from the classical theory of the buckling of cylindrical shells [see e.g. Yamaki (1984)], the most unstable circumferential buckling wavenumber increases as the tube length is decreased. The same effect can be seen in our problem. Figure 6 shows a diagram of the critical parameter combinations for the $L/R_0 = 10$ case for various values of the circumferential buckling wavenumber $N$. In the experimental set-up described above (increase the volume flux to the critical value while keeping the upstream pressure constant), the most unstable curve is the leftmost one. For small values of the upstream pressure, the most unstable buckling wavenumber is $N = 2$. For increasing upstream pressure (and increasing critical volume flux) the higher wavenumbers become unstable first. The diagram shows that for the value of $p_{\text{entry}}$, corresponding to the tube shown in the lower part of Figure 5, the most unstable wavenumber is in fact $N = 4$. The tube would already buckle at a value of $q_{\text{crit}} = 2 \cdot 98 \times 10^{-3}$ with $N = 4$ waves in the circumferential direction. Figure 7 shows the corresponding pre-buckling deformation and the buckling mode. Due to the lower critical volume flux for the $N = 4$ case, the compressed fraction of the tube is smaller than for the $N = 2$ case and the buckling is confined to the last quarter of the tube length.

Figure 8 shows the diagram of the critical parameter combinations for a longer tube with $L/R_0 = 20$. It can be seen that the transition to the higher buckling wavenumbers
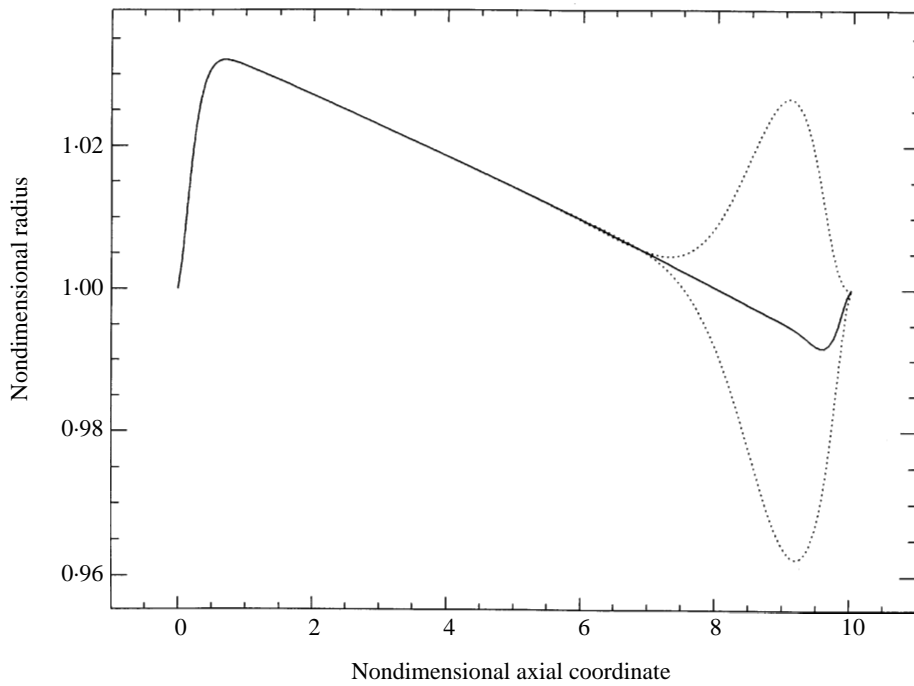
Figure 7. The pre-buckling deformation and buckling modes for a tube with $L/R_0 = 10$ under high upstream pressure, $p_{entry} = 2 \cdot 45 \times 10^{-3}$; $q_{crit} = 2 \cdot 98 \times 10^{-3}$. The high upstream pressure confines the buckling of the tube to the last quarter of its length. The corresponding most unstable wavenumber is $N = 4$.
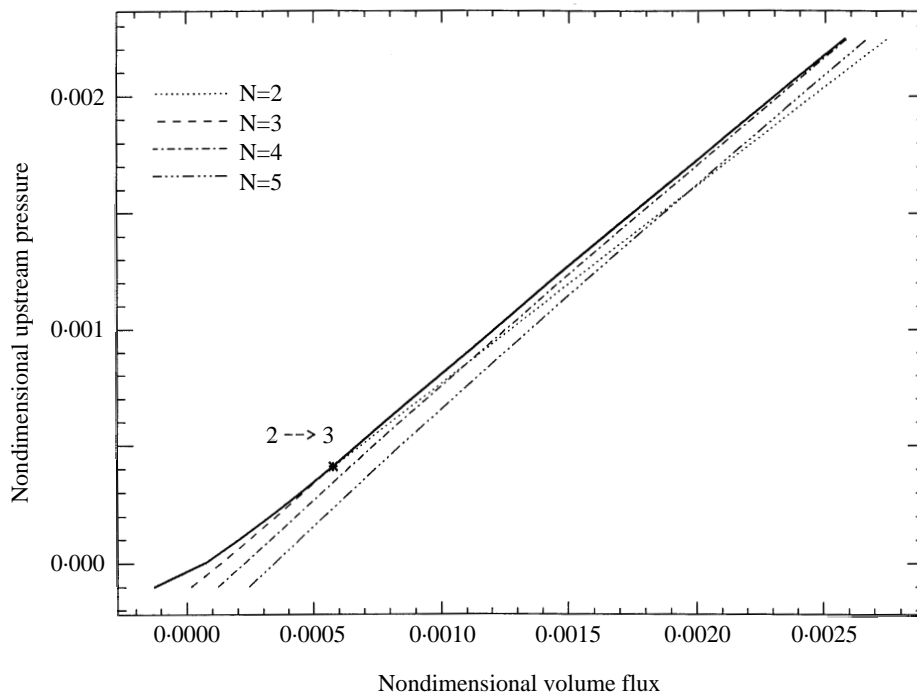


Figure 8. The critical parameter combinations for a tube with $L/R_0 = 20$.

is delayed to higher values of the upstream pressure. Again, this is due to the fact that the transition between the most unstable buckling wavenumbers is related to the length of the compressed part of the tube. An examination of the buckling modes shows that for both geometries the transition between $N = 2$ and $N = 3$ occurs when the length $L_{buckl}$ of the collapsing part of the tube is about $L_{buckl} \simeq 9R_0$. For the shorter tube only a small upstream pressure $p_{entry}$ is required to distend the first 10% of the tube length. For the longer tube, a significantly higher upstream pressure is required to keep more than 50% of the tube's upstream length distended.

In this context it should be noted that the volume flux parameter, $q$, is based on the nondimensional pressure drop through the undeformed tube and contains the ratio $L/R_0$. Therefore, the volume flux, $\dot{V}$, corresponding to identical values of $q$ in Figures 6 and 8 differs by a factor of two. For a given upstream pressure, longer tubes buckle at a lower value of the dimensional volume flux, $\dot{V}$.

Since veins and arteries in the human body are under pre-tension [they contract by up to 40% when they are cut; see Bergel (1972)], experiments have been carried out with axially pre-stretched tubes. The effects of axial pre-stretch can be examined with our model by prescribing nonzero axial displacements of the tube at the upstream and downstream ends.

As discussed in Heil & Pedley (1995a), the axial pre-stretch has two opposing effects. The increased axial tension makes the tube stiffer. However, the axial pre-stretch also reduces the tube's cross-sectional area due to the Poisson effect (the rubber tubes used in the experiments are nearly incompressible). The reduced cross-sectional area increases the tube resistance and thereby increases the compressive load on the tube wall.

These two effects lead to an interesting change in the stability of the tubes as the upstream pressure is increased. The lines in Figure 9 show the critical parameter
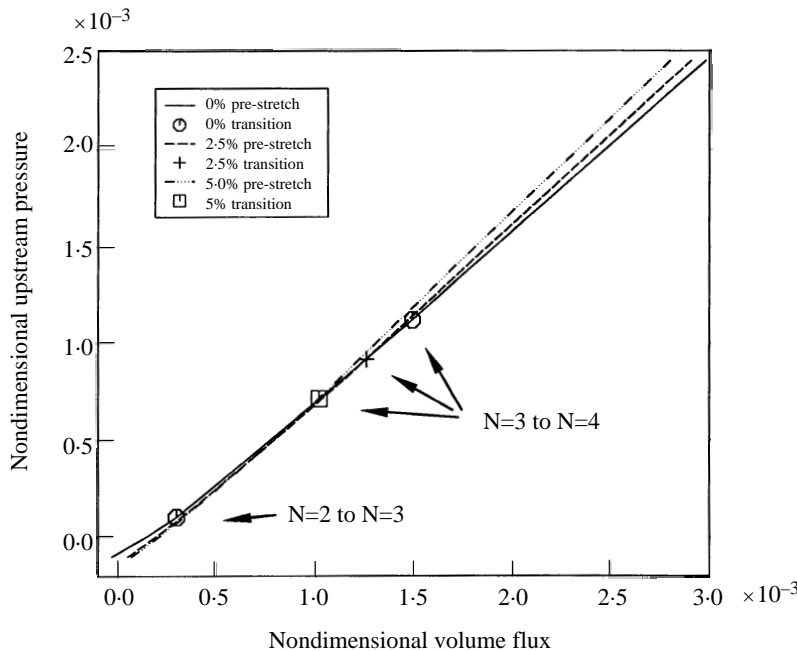


Figure 9. The most unstable parameter combinations for tubes with $L/R_0 = 10$ for different values of the axial pre-stretch. $\varepsilon_U = U/R_0 = 0$, 0·25, 0·5, corresponding to 0%, 2·5% and 5% axial pre-stretch. Only the most unstable combinations are shown and the transition between the most unstable wavenumbers is indicated by markers.

combination for a tube with $L/R_0 = 10$, subject to different values of the axial pre-stretch. For vanishing volume flux, the axial pre-stretch is clearly stabilizing and the curves for the pre-stretched tubes lie below the one for the unstretched tube.

For moderately large upstream pressure, the unstretched tube buckles at a lower value of the volume flux than the pre-stretched tubes. However, as the upstream pressure increases, the pre-stretched tubes become more unstable in the sense that, in the experiment described above, they buckle at a lower value of the volume flux than the unstretched tube—the pre-stretch seems to destabilize the system.

This apparent contradiction can be resolved by an examination of the axisymmetric pre-buckling deformation and the corresponding pressure distribution at the onset of buckling. This shows that, at the onset of buckling, the pre-stretched tube is, in fact, under a higher compressive load than the corresponding unstretched tube at the same value of the upstream pressure. Therefore, from a purely solid mechanics point of view, a pre-stretched tube is indeed ''more stable'' than an unstretched one, as one would expect.

However, for a given value of the upstream pressure, the resistance of a pre-stretched tube is higher than that of an unstretched tube since its cross-sectional area is reduced by Poisson's effect. For sufficiently high values of the volume flux, the destabilization due to the increase in the compressive load on the tube wall is stronger than the stabilization due to the axial pre-stretch.

Figure 9 also shows that the axial pre-stretch moves the transition to higher buckling wavenumbers to lower values of the upstream pressure.

Finally, we note that the iteration procedure described in Section 4.3 occasionally converged to a buckling mode with a higher number of axial waves, like the one shown in Figure 10. Obviously, the numerical procedure does not allow us to prescribe the
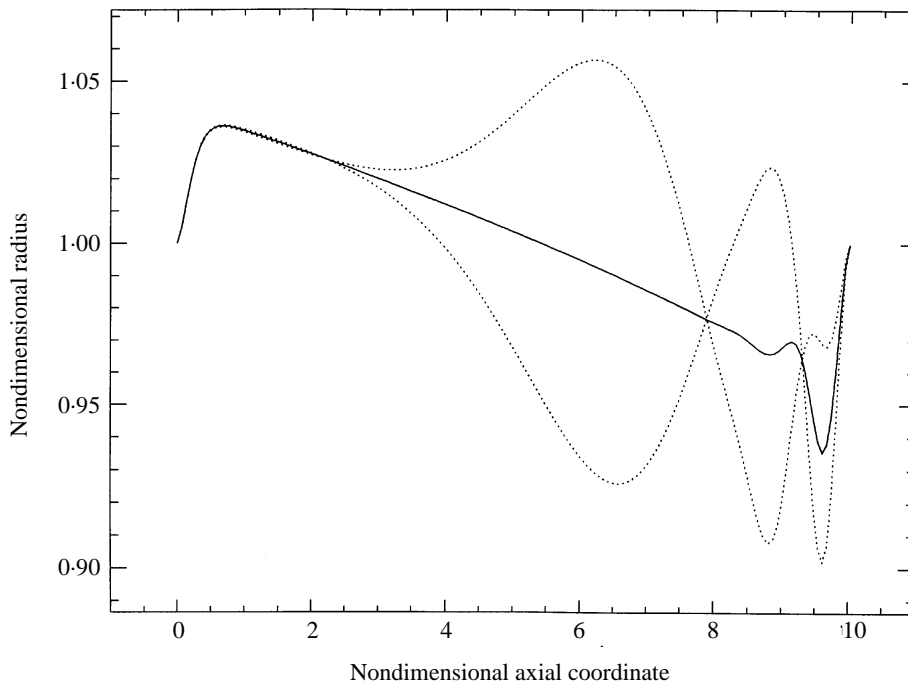


Figure 10. Buckling with a higher number of axial waves. $L/R_0 = 10$, $\varepsilon_U = 0$, $p_{\text{entry}} = 2 \cdot 96 \times 10^{-3}$ and $q_{\text{crit}} = 5 \cdot 35 \times 10^{-3}$.

number of axial waves in the buckling modes (as one could in a Galerkin method based on a Fourier expansion of the buckling modes in the axial direction). However, these instabilities were located in the unstable region and the buckling modes with one axial wave appear to be the most unstable ones. In fact, the buckling modes with higher axial wavenumbers were only obtained from iterations in which the initial guess for the volume flux, $q_0$, had been chosen too high.

For all cases presented in this study, the tube-wall slope at the onset of buckling was small enough to justify the use of lubrication theory for small Reynolds numbers (typically $\tan \alpha_{\max} = \mathcal{O}(10^{-2})$ at either the upstream or the downstream end for the most strongly collapsed tubes). Even for the strongly deformed tube shown in Figure 10, the maximum wall slope is only $\tan \alpha_{\max} = 0\cdot27$. The maximum strains in the axial and circumferential direction were approximately 5%; therefore the linear constitutive equations can be expected to provide an adequate description of the tube's stress-strain relationship.

## 6. CONCLUSIONS

We have investigated the linear stability of cylindrical shells conveying a viscous flow using geometrically nonlinear shell theory and lubrication theory. The buckling mechanism has been examined for an experimental procedure in which the upstream pressure is held at a constant value while the volume flux is increased until buckling occurs. It has been shown how variations of the upstream pressure, the tube geometry and the axial pre-stretch affect the tube stability and its buckling deformation.

The results presented have been shown to be consistent with the small strain assumption used in the constitutive equations and with the small wall-slope assumption used in the simplification of the fluid equations. Hence, we expect them to be accurate for small Reynolds numbers.

The results of the parameter studies (critical combination of upstream pressure and volume flux and the wavenumber of the most unstable buckling mode) define the starting points for the examination of the large displacement postbuckling behaviour presented in Heil & Pedley (1995b).

## ACKNOWLEDGEMENTS

REFERENCES

ALMROTH, B. O. 1966 Influence of edge conditions on the stability of axially compressed cylindrical shells. *AIAA Journal* **4,** 134–140.
BERGEL, D. H. 1972 The properties of blood vessels. In *Biomechanics. Its Foundations and Objectives* (eds Fung, Y. C., Perrone, N. & Anliker, M.) New Jersey: Prentice-Hall.

CONRAD, W. A. 1969 Pressure-flow relationships in collapsible tubes. *IEEE Transactions on Biomedical Engineering* BME-**16,** 284–295.

ELAD, D., SAHAR, M., AVIDOR, J. M. & EINAV, S. 1992 Steady flow through collapsible tubes: measurements of flow and geometry. *ASME Journal of Biomechanical Engineering* **114,** 84–91.

HEIL, M. & PEDLEY, T. J. 1995a Large axisymmetric deformations of a cylindrical shell conveying a viscous flow. *Journal of Fluids and Structures* **9,** 237–256.

HEIL, M. & PEDLEY, T. J. 1995b Postbuckling deformation of a cylindrical shell conveying a viscous flow. Submitted to *Journal of Fluids and Structures.*

KAMM, R. D. & PEDLEY, T. J. 1989 Flow in collapsible tubes: a brief review. *ASME Journal of Biomechanical Engineering* **111,** 177–179.

KATZ, A. I., YU CHEN & MORENO, A. H. 1969 Flow through a collapsible tube: experimental analysis and mathematical model. *Biophysical Journal* **9,** 1261–1279.

LOWE, T. W. 1994 Private communication.

LOWE, T. W. & PEDLEY, T. J. 1995 Computation of Stokes flow in a channel with a collapsible segment. *Journal of Fluids and Structures,* **9,** 885–905.

PAIDOUSSIS, M. P. & DENISE, J.-P. 1972 Flutter of thin cylindrical shells conveying fluid. *Journal of Sound and Vibration* **20,** 9–26.

PAIDOUSSIS, M. P. & LI, G. X. 1993 Pipes conveying fluid: a model dynamical problem. *Journal of Fluids and Structures* **7,** 137–204.

PEDLEY, T. J. 1980 *The Fluid Mechanics of Large Blood Vessels.* Cambridge: Cambridge University Press.

PRESS, W. H., TEUKOLSKY, S. A., VETTERLING, W. T., FLANNERY, B. P. 1992 *Numerical Recipes in FORTRAN,* 2nd edition. Cambridge: Cambridge University Press.

SANDERS, J. L. 1963 Nonlinear theories for thin shells. *Quarterly of Applied Mathematics* **21,** 21–36.

WEMPNER, G. 1973 *Mechanics of Solids.* New York: McGraw-Hill.

WILD, R., PEDLEY, T. J. & RILEY, D. S. 1977 Viscous flow in collapsible tubes of slowly-varying elliptical cross-section. *Journal of Fluid Mechanics* **81,** 273–294.

YAMAKI, N. 1984 *Elastic Stability of Circular Cylindrical Shells.* Amsterdam: North-Holland.

## APPENDIX: WARPING OF THE CROSS-SECTION IS A SECOND-ORDER EFFECT

In this appendix we shall show that the warping of the cross-sections due to the axial component of the buckling displacements can be neglected in the transformation between Eulerian and Lagrangian coordinates. For simplicity we neglect the effect of the wall thickness in the following analysis. We denote the order of magnitude of the buckling displacements by $\varepsilon \ll 1$.

Let us examine the deformation of the tube in two steps. During the axisymmetric pre-buckling deformation, material points which were in a plane $z = x^1$ in the undeformed configuration (thin lines in the left half of Figure 11) are displaced to a new position $z_{\text{axisym}}(x^1) = x^1 + v_A^1(x^1)$ and they remain in one plane (thick lines in the left half of Figure 11). In Section 2.2 we used this transformation to establish a mapping between the axial Eulerian and Lagrangian coordinates before the buckling. In the axisymmetric prebuckling configuration the Eulerian polar angle $\varphi$ and the radius $R$ of a point in the cross-section $z_{\text{axisym}}(x^1)$ depend only on the circumferential Lagrangian coordinate $x^2$—in fact we have $\varphi = x^2$ and $R = \text{const.}$

Once the tube buckles, the axial component of the buckling displacement, $v_B^1 = V_B^1(x^1)\cos(Nx^2) = \mathcal{O}(\varepsilon)$, moves material points, which were originally in one plane, to different axial coordinates. A cross-section $z = \hat{z}$ contains material points which were separated by a distance $\delta z = 2V_B^1 = \mathcal{O}(\varepsilon)$ in the pre-buckling configuration (see right half of Figure 11). Let us denote the difference in the axial Lagrangian coordinates of the points in the cross section $z = \hat{z}$ by $\delta x^1$. For moderate axial strains we have $\delta x^1 \simeq \delta z = \mathcal{O}(\varepsilon)$.

The radial distance to a material point on the tube's surface is $R = v_A^3(x^1) + V_B^3(x^1)\cos(Nx^2)$. Therefore, the difference in the radial displacement due to the warping is

$$\delta R = \left[\frac{\partial v_A^3}{\partial x^1} + \frac{\partial V_B^3}{\partial x^1}\cos(Nx^2)\right]\delta x^1. \tag{67}$$
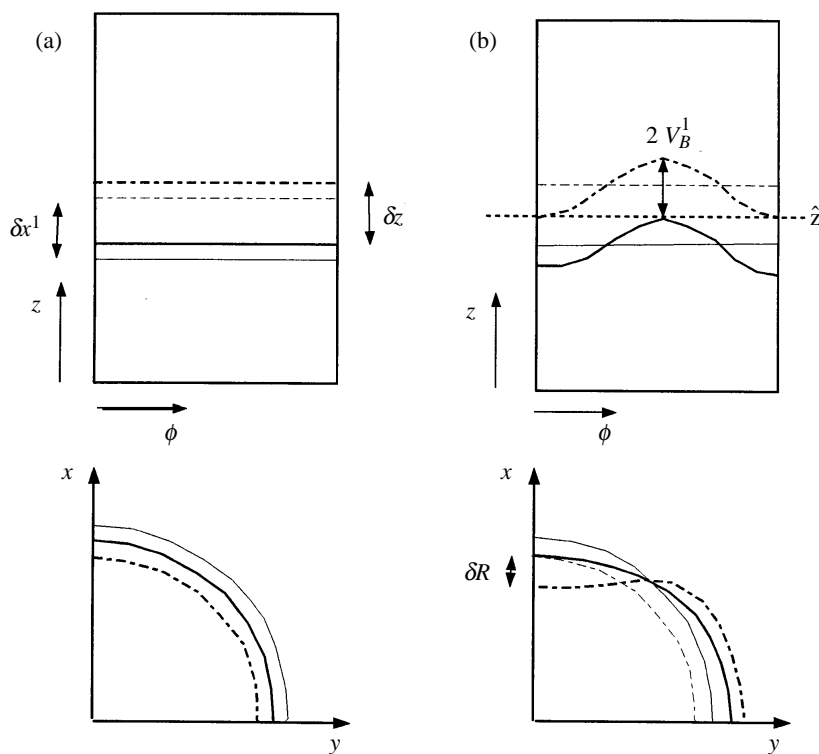
Figure 11. Sketch illustrating the warping of the cross-sections during buckling. Due to the axial component of the buckling displacement, a cross-section $z = \hat{z}$ in the buckled configuration contains material points which were separated by a distance $\delta x^1$ in the undeformed configuration. In (a): thin lines are for the undeformed wall, thick lines for axisymmetric deformation. In (b): thin lines are for axisymmetric deformation, while thick lines are for the buckled wall.

Since $\partial V_B^3/\partial x^3 = \mathcal{O}(\varepsilon)$, the change in the tube's radius is a second order effect provided

$$\frac{\partial v_A^3}{\partial x^1} = \mathcal{O}(\varepsilon), \tag{68}$$

which is consistent with the small slope assumption used in the simplification of the fluid equations.